Polarized scattering by Gaussian random particles under radiative torques

Joonas Herranen[a,*], Johannes Markkanen[a], Karri Muinonen[a,b]

[a]*Department of Physics, University of Helsinki, Finland*
[b]*Finnish Geospatial Research Institute FGI, National Land Survey, Finland*

Abstract

We study the internal alignment of a statistical ensemble of Gaussian random ellipsoids with respect to the radiation direction. We solve the rigid body dynamics due to scattering forces and torques, using a numerically exact and efficient T-matrix solver for arbitrary particle shapes and compositions. We then compare the polarization of the aligned ensemble to a randomly oriented ensemble and a perfectly aligned ensemble. We find that the ensemble becomes partially aligned under monochromatic radiation and that the internal alignment has an significant effect on the intensity and polarization of the scattered light.

Keywords: Gaussian random shapes, Radiative torque, Polarization, Dynamical alignment
2010 MSC: 00-01, 99-00

1. Introduction

Understanding the statistical behavior of dust is crucial in interpretation of observational results and in the tackling of inverse problems, such as deducing magnetic field properties from observed polarization [1] or dust properties in general.

Aligned dust particles were shown to be the cause of interstellar polarization in the near-infrared and the visible light regimes in 1949 independently by Hall and Hiltner [2, 3]. In a few years, the discussion about the causes of alignment were started by Davis and Greenstein [4]. In the following several decades, the dominating mechanism of alignment was debated, until radiative torques became the leading explanation to observations, with other effects contributing in different local environments [5, 6].

Even though the subtle interactions causing many local abnormalities in the observation data are understood better than ever (see current state in [7, 8] and references therein), much groundwork in understanding the observations can still be done. For example, statistical modeling of the effect of dust dynamics on polarization has been an unreachable computational effort until recent years.

In this work, our aim is to illustrate the effect of scattering of light from dust particles to the polarization of dust using state-of-the-art numerical scattering methods. We focus on the bare problem on the effect of scattering only to the dynamics, leading the way to addition of several physical processes found in the interstellar environment, e.g. gas bombardment, Larmor precession and paramagnetic relaxation [7]. We model solid dust particles using Gaussian random shapes [9, 10]. The reaction of the particles to the scattering of different wavelengths is studied by numerically integrating the equations of motion. The results are then used to create an ensemble average of the scattering matrix describing angle-dependent intensity and polarization.

To the best knowledge of the authors, such numerically exact methods have never been applied in the same scale for dynamical systems.

2. Theory of scattering dynamics

In this work, the combination of rigid body dynamics, electromagnetic scattering, and radiative forces and torques are shortened as scattering dynamics. In scattering dynamics, we will solve the equations of motion for a dust particle through direct step-by-step calculations. This is possible for

*Corresponding author
Email address: joonas.herranen@helsinki.fi (Joonas Herranen)

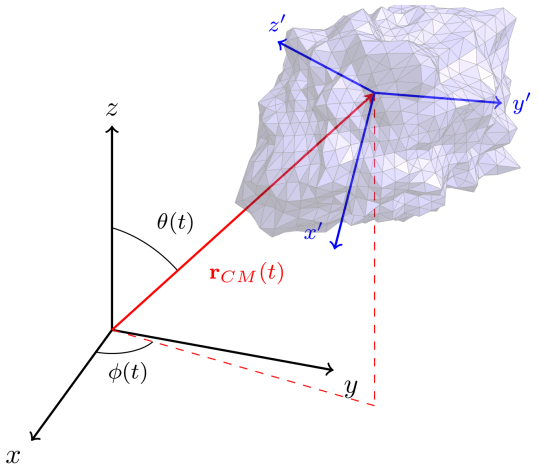

Figure 1: The position of a tetrahedral model of a solid particle with its principal axes with respect to the laboratory coordinates. Each tetrahedron is handled with respect to the principal axis coordinates. Orientation can be handled in the plane wave case separately with e.g. using rotation matrices, describing the orientation of the principal axes w.r.t. to the laboratory frame axes.

an arbitrary particle through a fast and accurate way of solving the T-matrix of scattering.

In the following subsections, the relevant physics in scattering dynamics is reviewed.

2.1. Dynamics of a rigid body

A rigid body can be used to model a dust particle in almost any conceivable situation. Even in such situations, where a real dust particle would deform or break, the change in the inertia parameters of the particle can be modeled. These situations would, of course, change also the corresponding scattering problem so that methods introduced later would face considerable problems. For this, and the simplicity of notation, we will focus on the theory of a strictly rigid body in our model.

The particle may be a single solid particle, such as illustrated in Figure 1, or an aggregate. For the purposes of the scattering solver, the solid particles are discretized as tetrahedral meshes, where each tetrahedron is homogeneous. In both cases, the inertia parameters of the particle are solved using the parallel axis theorem. Method of reference tetrahedra [11] simplifies the calculation of the moment of inertia tensor of an arbitrary tetrahedron.

Diagonalization of the moment of inertia tensor gives the so-called principal axes of the particle. Principal coordinates are a type of body coordinates who coincide with the principal axes. Thus, the principal coordinate system is defined with respect to the laboratory coordinates by an orientation matrix

$$\mathbf{P} = \begin{pmatrix} P_{1,x} & P_{2,x} & P_{3,x} \\ P_{1,y} & P_{2,y} & P_{3,y} \\ P_{1,z} & P_{2,z} & P_{3,z} \end{pmatrix} = (\mathbf{a}_1\, \mathbf{a}_2\, \mathbf{a}_3), \quad (1)$$

where column vectors $\mathbf{a}_i$ are the principal axes of the particle from smallest moment of inertia to largest. The equations of rotational motion are simplified into Euler's equations in the principal axes, and they are the usual choice for solving rotational dynamics.

2.2. Electromagnetic forces and torques

For a general description of scattering, the most important quantities are the size parameter of the particle, $x = ka = 2\pi a/\lambda$, the shape and the complex index of refraction $n = n_{Re} + in_{Im}$ of the particle. Above, a is the equivalent radius of the particle to a sphere of the same volume, k is the wavenumber, and λ the wavelength of the incident radiation. Usually, the dimensionless size parameter is enough to describe many interesting quantities. However, in order to make sense of the dynamical time scales, it is temptating to choose a concrete size and density for the particle and fix the wavelengths to correspond to certain size parameters.

In space environments, the incident radiation from starlight is mostly visible and infrared light, and can be modeled as plane waves. Regarding dust in space, a wavelength range of 200–2000 nm corresponds to size parameter range 0.03–30 for particles ranging from 0.01 μm to 1 μm in equivalent radius.

The mechanical effects of radiation are described by the Maxwell stress tensor, T, which should not be confused with the T-matrix. The Maxwell stress tensor has components

$$T_{ij} = \varepsilon_0 \left(E_i E_j - \frac{1}{2}\delta_{ij} E^2 \right) + \frac{1}{\mu_0} \left(B_i B_j - \frac{1}{2}\delta_{ij} B^2 \right). \quad (2)$$

For almost all intents and purposes the term with the Maxwell stress tensor dominates the total force in a volume V,

$$\mathbf{F} = \oint_S \mathsf{T} \cdot \hat{\mathbf{n}} \mathrm{d}S - \varepsilon_0 \mu_0 \int_V \frac{\partial}{\partial t} \mathbf{S} \mathrm{d}V, \quad (3)$$

where S is the surface of V, where momentum transfer is occuring. This is due to the fact, that the latter term describes the momentum contained

within the volume instead of being transferred into it. The latter term, containing the Poynting vector $\mathbf{S}$, varies with the frequency of the radiation, and thus for most applications, will be averaged out of consideration [12].

After averaging, total force and torque will be represented by simple surface integrals containing the Maxwell stress tensor,

$$\begin{aligned} \mathbf{F} &= \oint_S \mathsf{T} \cdot \hat{\mathbf{n}} \, \mathrm{d}S, \\ \mathbf{N} &= \oint_S \mathbf{r} \times (\mathsf{T} \cdot \hat{\mathbf{n}}) \, \mathrm{d}S. \end{aligned} \tag{4}$$

The torque obtained by solving the scattering problem can be written in terms of normalized quantities [13] as

$$\mathbf{N} = \frac{\lambda a^2}{2c} \langle S \rangle_{\mathrm{inc}} \mathbf{Q}_{\mathbf{N}}, \tag{5}$$

where $\langle S \rangle_{\mathrm{inc}}$ is the incident Poynting vector, and $\mathbf{Q}_{\mathbf{N}}$ is the normalized quantity, the torque efficiency. In particular the torque efficiency can be used to compare results between different geometries with the same consistency.

2.3. The solution of the scattering problem

Solving the scattering problem is to simply write the scattered field in terms of the incident field using knowledge about the scatterer.

The incident and scattered fields can be expanded in terms of vector spherical wave functions (VSWFs),

$$\begin{aligned} E^{\mathrm{inc}} &= \sum_{n=1}^{\infty} \sum_{m=-n}^{n} a_{nm} \mathbf{M}_{nm}^{\mathrm{inc}} + b_{nm} \mathbf{N}_{nm}^{\mathrm{inc}}, \\ E^{\mathrm{sca}} &= \sum_{n=1}^{\infty} \sum_{m=-n}^{n} p_{nm} \mathbf{M}_{nm}^{\mathrm{sca}} + q_{nm} \mathbf{N}_{nm}^{\mathrm{sca}}, \end{aligned} \tag{6}$$

where $\mathbf{M}_{nm}^{\mathrm{inc/sca}}, \mathbf{N}_{nm}^{\mathrm{inc/sca}}$ are the incident and scattered VSWFs based on spherical Bessel functions and Hankel functions of the first kind, with expansion coefficients a_{nm}, b_{nm}, p_{nm}, and q_{nm}. There is some freedom in choosing the explicit form of the expansion, some standards can be found in e.g. [14, 15]. This treatment allows the analytical calculation of the integrals in (4) [16]. A VSWF expansion thus paves the way for applying the T-matrix method in the calculation of forces and torques with ease.

In the T-matrix formulation, the T-matrix of the scatterer gives the relation between the scattered and incident VSWF coefficients,

$$\tilde{\mathbf{p}} = T\tilde{\mathbf{a}}, \tag{7}$$

where all scattered and incident VSWF coefficients are collected into vectors $\tilde{\mathbf{p}}$ and $\tilde{\mathbf{a}}$.

The most difficult part of the problem is to find the T-matrix for the scatterer. For some simple geometries, such as smooth ellipsoids, efficient methods can be formulated, but for arbitrary shapes, or even cubes, usual point-matching methods will often have problems. In these cases, numerical methods may be used [17, 18].

We calculate the T-matrix using the electric current volume integral equation (JVIE) formulation of scattering [19], which is an efficient approach for even strongly inhomogeneous scatterers. The JVIE formulation is then used to solve the T-matrix by linking the discretization basis function coefficients of JVIE with the VSWF expansion coefficients of the T-matrix method [20].

As the T-matrix solves scattering with arbitrary incident VSWF expanded fields, the problem of a spinning dust particle can simply apply the usual rotation formulae for the expansion coefficients [21]. The complete solution requires transformations between frames of reference.

3. Polarization by aligned Gaussian random shapes

The goal of this work is to study, how unpolarized light gets polarized under scattering from aligned dust particles, modeled as a statistical ensemble of Gaussian random shapes. The simulated situation is reduced to laboratory conditions: instead of studying a realistic wavelength band, we focus on polarization effect on certain single ratios of particle size and wavelength, or size parameters.

3.1. Measures of polarization

The polarization state of light can be encoded into a Stokes vector $\mathbf{I} = (I, Q, U, V)^{\mathsf{T}}$, whose components are called the Stokes parameters. The parameter I is proportional to the total flux, whereas Q and U describe the state of linear polarization, and V the state of circular polarization.

With disregard to coherence, a complete picture of polarization under interactions is given by the

Mueller matrix. The Mueller matrix maps the incident Stokes vector to a transmitted Stokes vector [22]. The Mueller matrix for a single scattering process is also called simply a scattering matrix, which we will also refer to henceforth.

The scattering matrix is a 4×4-matrix, the columns of which describe, how the unpolarized, horizontal-vertical polarized, $\pm 45°$-polarized and circularly polarized components transform under scattering. It is well-known, that for a mixture of randomly oriented particles with equal amount of mirror image particles, the scattering matrix becomes block-diagonal with 6 independent elements [23]:

$$\begin{pmatrix} S_{11} & S_{12} & 0 & 0 \\ S_{12} & S_{11} & 0 & 0 \\ 0 & 0 & S_{33} & S_{34} \\ 0 & 0 & -S_{34} & S_{44} \end{pmatrix}. \tag{8}$$

From the shape of the above scattering matrix, it is obvious that unpolarized incident radiation will become linearly polarized.

3.2. Gaussian random spheres and ellipsoids

For modeling the shapes of irregular particles we use Gaussian random shapes, either spheres [9] or ellipsoids [10], such as illustrated in Figure 2. The radius statistics for the spheres are drawn from a lognormal distribution, and can be generated using a spherical harmonics expansion for the radius, and a Legendre expansion for its autocorrelation function. The defining parameters of the spheres are thus the standard deviation σ and the correlation lenght l. For the ellipsoids, an extension of the sphere, two additional shape parameters are needed: the axial ratios $a : b$ and $b : c$.

3.3. Polarization by aligned particles

Aligned particles refer in this work to particles in a stable rotational motion, where the angular velocity vector and one of the principal axes of the particle is pointing to a small angular window. This is more exactly called internal alignment, as an external reference direction is yet to be introduced. Under radiation, both internal and external alignment have been shown to occur in interstellar dust [5, 24]. Moreover, alignment happens preferably to the principal axis of the highest moment of inertia, Q_3, as it resists any perturbation the most, be it by torques or dissipation of rotational energy.

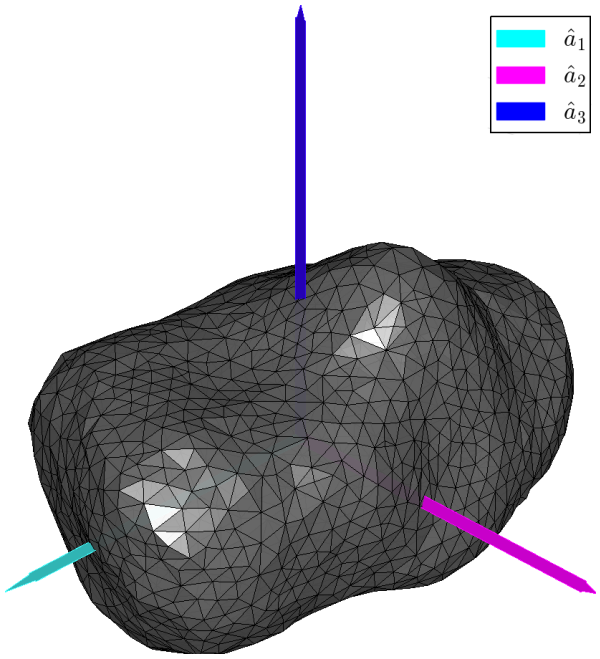

Figure 2: An example of a Gaussian random ellipsoid, represented as a tetrahedral mesh, with $\sigma = 0.125$, $l = 0.35$ and $a : b : c = 1 : 0.8 : 0.6$.

When dust particles are systematically aligned, the observables in comparison with randomly oriented particles will change in many ways. The scattering matrix will lose some of its symmetry properties, particularly the 2×2 block off-diagonals can become non-zero. Thus, alignment is one mechanism how an unpolarized incident beam can obtain a circularly polarized component. This circular polarization due to scattering effects has been demonstrated in the past using semianalytical methods [7].

4. Numerical Methods

We apply a Fortran software for solving the equations of motion for an inhomogeneous particle, discretized by either tetrahedral meshing, which has been developed by the authors. The software analyses the mesh geometry, then calculates the inertia parameters and the T-matrix of the scatterer. The T-matrix is determined by an implementation of the JVIE T-matrix method, abbreviated as T-VIE [25].

The dynamical simulation is run until the situation is evolved a predefined number of time steps, N_{steps}, or until internal alignment of the principal

axis of largest moment of inertia, $\mathbf{a}_3$, occurs. Then, the Mueller matrix components are solved as the average from the last 1.5 percent of the run. For comparison, Mueller matrices of randomly oriented and perfectly aligned particles are created.

Perfect alignment refers here to the situation, where $\mathbf{a}_3$ and angular velocity ω are perfectly parallel to each other and perpendicular to the wave vector $\mathbf{k}$ of the incident radiation, directed along the z-axis of the laboratory frame. Also, in all cases, an artificial external alignment is introduced by rotating the situation so that the average of ω has an (x, y)-projection $(1, 0)$. This is done to introduce another external direction, which with $\mathbf{k}$ is needed to analyse alignment at all.

5. Results

An ensemble of 60 homogeneous Gaussian ellipsoids, composed of 15 ellipsoids, oblate spheroids, prolate spheroids, and spheres each, described in Figure 3, with size parameters $ka = \{0.3, 1, 3\}$ and complex refractive indices $n = \{1.31 + \mathrm{i}0.0, 1.70 + \mathrm{i}0.0, 2.0 + \mathrm{i}0.2\}$, corresponding ice, silicate and organic compounds, often assumed to be contained in cosmic dust. Geometries were evolved for $N_{\mathrm{steps}} = 1 \cdot 10^7$ timesteps under unpolarized incident radiation.

Time stepping is adaptive, so that during a single timestep, a maximum rotation of 0.01 radians is allowed. The time scales in the calculations presented here are affected only by the incident Poynting vector, as the focus is solely on the dynamical effects of scattering. Taking inertia properties (inertia tensor I, volume V) of solid spheres, roughly the size of 1 μm and the wavelenght, and $\rho \sim 1000 \frac{\mathrm{kg}}{\mathrm{m}^3}$, a back-of-the-envelope calculation starting from $\Delta\omega \sim I^{-1}\mathbf{N}$ and (5) gives a rough approximation on the relation between the maximum rotation θ_{max} and the timestep Δt as, disregarding the SI-units,

$$\theta_{\mathrm{max}} \sim 100 \langle S \rangle_{\mathrm{inc}} \mathbf{Q}_{\mathbf{N}} \Delta t. \tag{9}$$

A typical torque efficiency can be of order 10^{-2}. Thus, if the incident planewave amplitude is set to unity, or $\langle S \rangle_{\mathrm{inc}} \approx 10^{-3} \frac{\mathrm{W}}{\mathrm{m}^2}$, the expected lenght of the simulation is several days of simulated time, at maximum.

The simulations were run in total 6 times, each with randomized initial orientation of the particle, to obtain an average alignment result for each particle.

Table 1: Values of $\log(C_{\mathrm{sca}})$ per particle for the 60 randomly oriented Gaussian particles (GE).

$n \backslash ka$	0.3	1.0	3.0
1.31+i0.0	-4.566	-1.752	0.628
1.7+i0.0	-4.162	-1.194	1.076
2.0+i0.2	-3.900	-0.933	0.773

After the dynamical simulation, alignment of the stable principal axes, $\mathbf{a}_1$ and $\mathbf{a}_3$, were observed. As a considerable fraction showed no alignment under this monochromatic situation, the ensemble is henceforth called imperfectly aligned. The internal alignment of the ensemble is summarized in Figure 4 histogrammatically. As the measure of alignment, the smallest angle between average directions of the stable principal axes and the angular velocity was chosen. This results, in many cases, in two separate distributions, of which the leftmost below about 30 degrees has the aligned particles, with precession about the angular velocity.As the angular velocity has greater oscillations than the angular momentum, averaging of highly unstable situations appear as more random noise in the histograms. In figure 5, the evolution of alignment is studied at 4 different times during the simulations. The times $t_1 - t_4$ are the situation at 10 000, 100 000, 1 000 000, and 10 000 000 timesteps, respectively. Gradual alignment is visible in all ensembles of different size parameters, with most alignment in the $ka = 3$ case.

First, in Figure 6, we compare the S_{11} and S_{12} components of all the randomly oriented particle scattering matrices of the smooth base geometries to the deformed Gaussian shapes. 500 random orientations are used for the calculations. Corresponding scattering cross sections C_{sca}, normalized to a single particle, are tabulated in Table 1. The smaller size parameters, $ka = 0.3$ and 1, show similar results as small spherical particles[22]. For the largest size parameter, $ka = 3$, smooth particles result in larger intensity to the backscattering directions. In all cases, the degree of linear polarization is very nearly the same.

Then, we compare the randomly oriented case and the imperfectly aligned case in Figures 7–11. The intensities are highly similar for all size parameters and shapes. The polarizations have visible, up to 10 percent differences, in all size parameters for the total ensemble average, in Figure 7. Cross sections per particle are found in Table 2. For the average of each geometry type, the largest difference

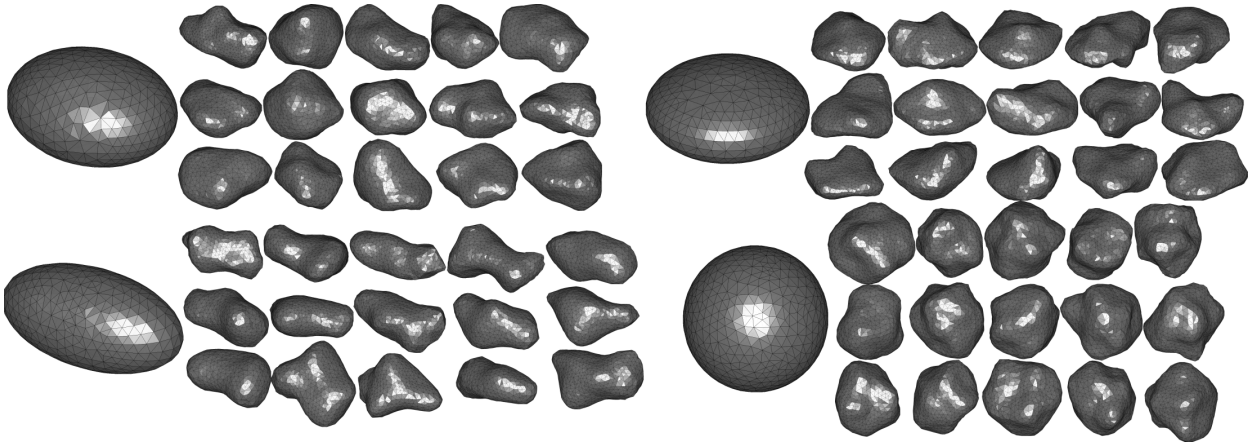

Figure 3: The Gaussian random shapes used in the simulation. All shapes are realizations of the Gaussian ellipsoid with $\sigma = 0.35$ and $l = 0.125$. Axial ratios $a : b : c$ are 1:0.8:0.6, 1:1:0.5, 1:0.5:0.5, and 1:1:0.99, corresponding to an ellipsoid, an oblate and a prolate spheroid, and a sphere, were chosen. The base shapes with 15 realizations of the Gaussian ellipsoid are in said order from top left to bottom right.

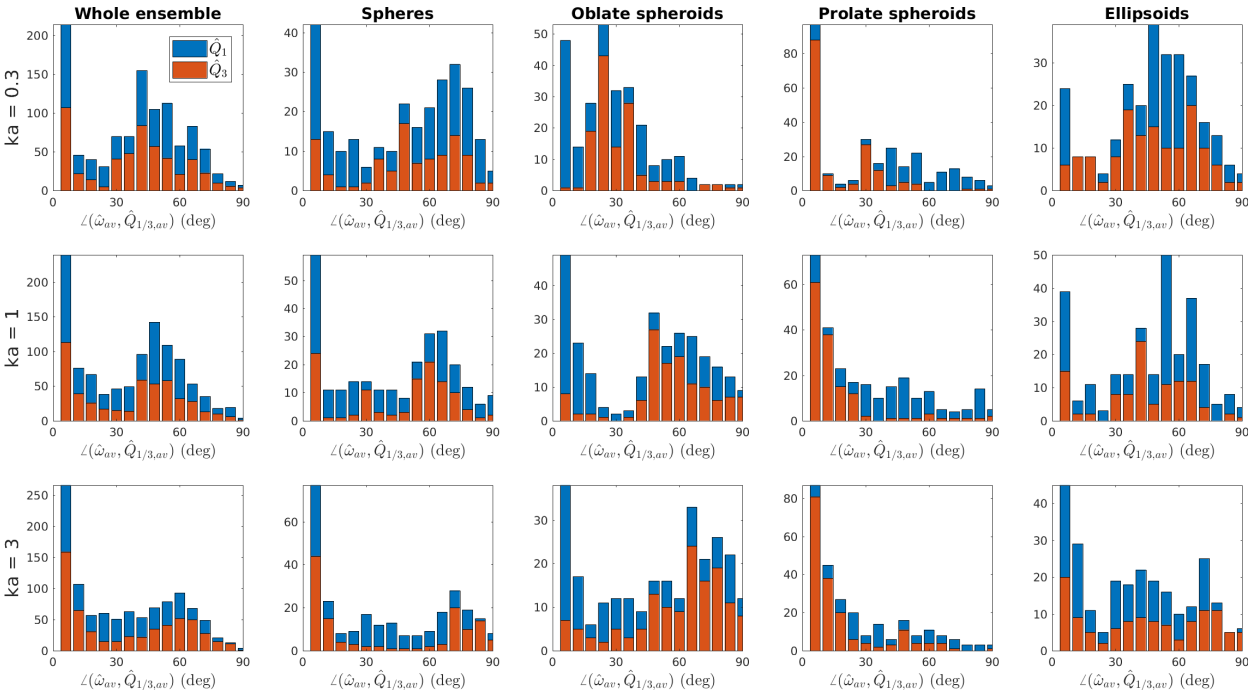

Figure 4: Internal alignment of the ensemble for each size parameter. The red bars correspond to the most stable state, alignment of $\mathbf{a}_3$ with respect to the angular velocity. Most aligned particles can be found in the case $ka = 3$. The prolate spheroids exhibit the most stable alignment, and the oblate spheroids the least alignment with much alignment of the non-preferred axis $\mathbf{a}_1$.

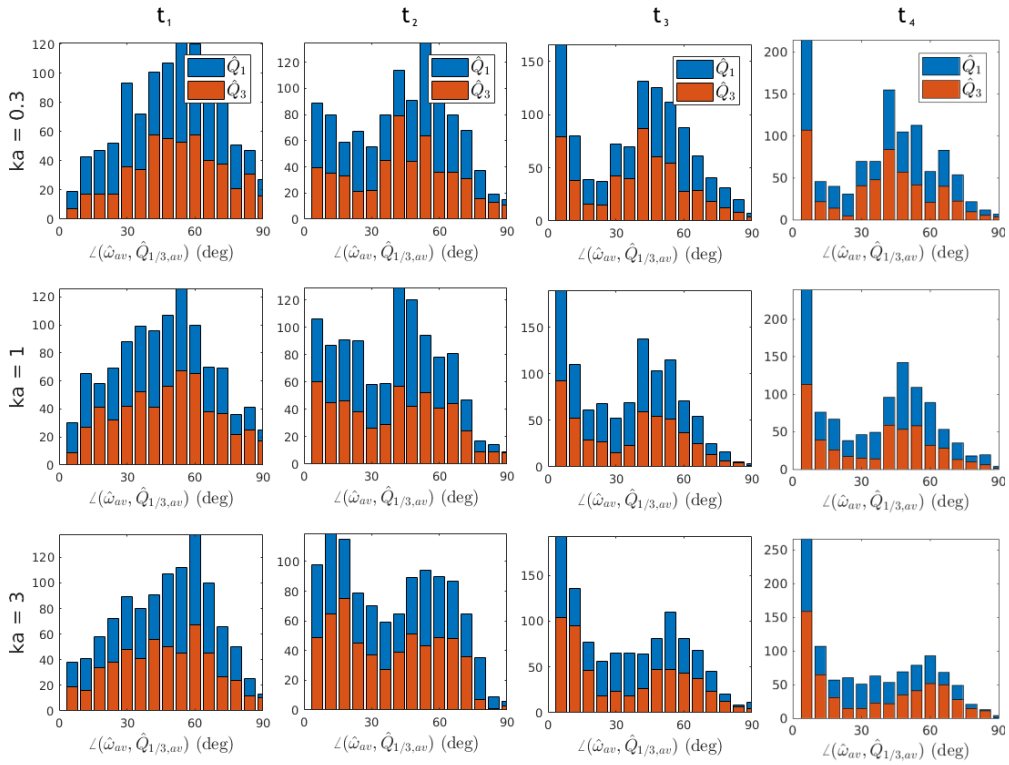

Figure 5: Evolution of the alignment of the whole ensemble, with same format as in Figure 4.

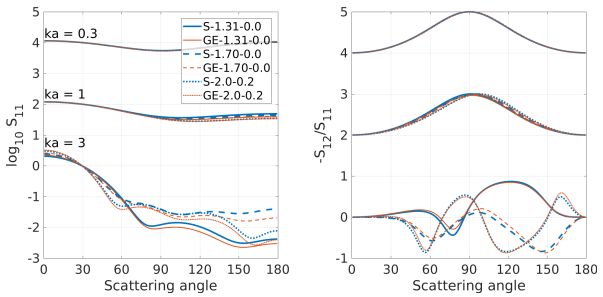

Figure 6: Comparison of averaged polarization between random orientations of the 4 smooth ellipsoids (S) and the 60 different Gaussian ellipsoids (GE). All curves have the same scale, with intensities additionally normalized to unity at $\theta = 30$ degrees. The curves of size parameters $ka = 0.3$ and 1 are shifted by steps of 2

Table 2: Same as Table 1, but for the imperfectly aligned (Al) case from Figure 7 for the whole ensemble of geometries.

$n\backslash ka$	0.3	1.0	3.0
1.31+i0.0	-4.314	-1.541	0.8041
1.7+i0.0	-3.972	-0.998	1.254
2.0+i0.2	-3.702	-0.7323	0.9731

Table 3: Same as Table 2, but for only the deformed spheres.

$n\backslash ka$	0.3	1.0	3.0
1.31+i0.0	-4.694	-1.754	0.818
1.7+i0.0	-4.069	-1.050	1.262
2.0+i0.2	-3.815	-0.790	0.891

is in the prolate spheroid case, in Figure 10, where also the highest level of alignment is observed.

Finally, we compare the imperfectly and perfectly aligned cases. The comparison is made in scattering planes, defined by the azimuthal angle $\phi = 0°, 1°, \ldots, 359°$, in the notation of [22]. The average scattering matrices are computed for the whole ensemble at the time, and the different refractive indices are separated into the Figures 12–14. The refractive index affects the general shape

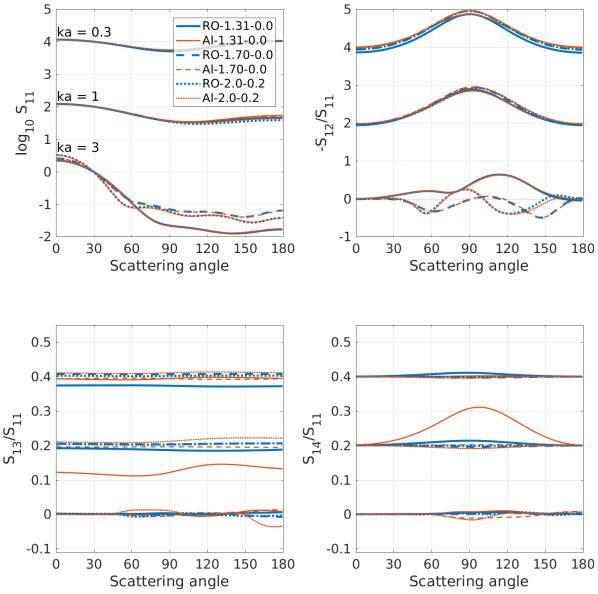

Figure 7: Comparison of the average scattering matrix elements for both randomly oriented (RO) and imperfectly aligned (Al) cases for all 60 deformed Gaussian shapes. Above 2 subplots as in Figure 6, but with additional 2 matrix elements, both shifted by 0.2.

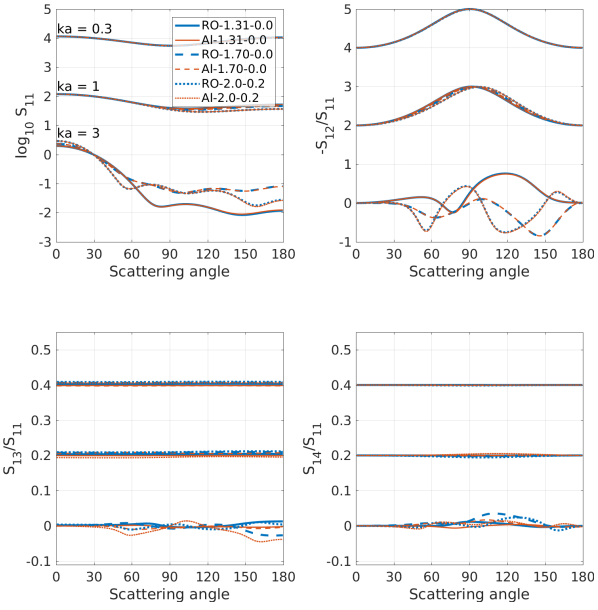

Figure 8: As in Figure 7, but for the 15 deformed spheres only.

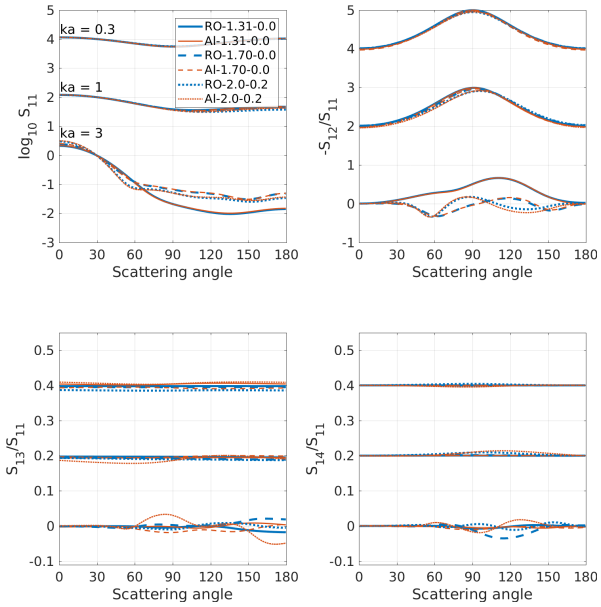

Figure 9: As in Figure 7, but for the 15 deformed oblate spheroids only.

Table 4: Same as Table 2, but for only the deformed oblate spheroids

$n\backslash ka$	0.3	1.0	3.0
1.31+i0.0	-4.689	-1.776	0.7961
1.7+i0.0	-4.043	-1.039	1.273
2.0+i0.2	-3.680	-0.728	1.023

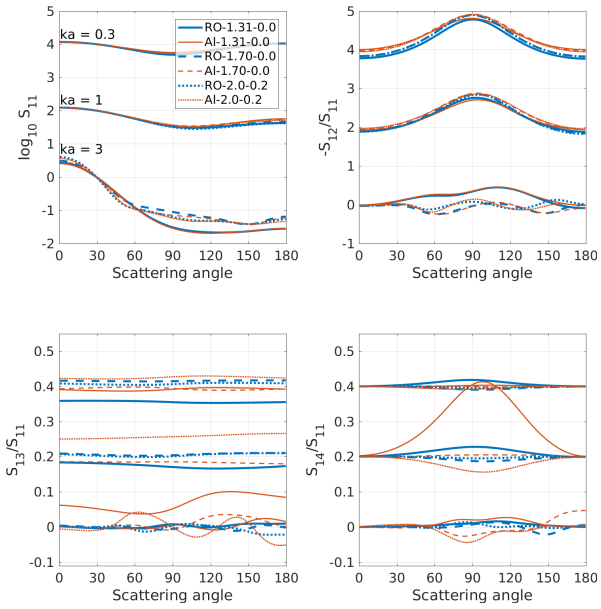

Figure 10: As in Figure 7, but for the 15 deformed prolate spheroids only. Note that in the S_{14}/S_{11} component, the solid red line of case $ka = 1$ overlaps the below curves of case $ka = 3$ slightly.

Table 5: Same as Table 2, but for only the deformed prolate spheroids

$n\backslash ka$	0.3	1.0	3.0
1.31+i0.0	-3.876	-1.199	0.797
1.7+i0.0	-3.788	-0.885	1.216
2.0+i0.2	-3.566	-0.658	0.988

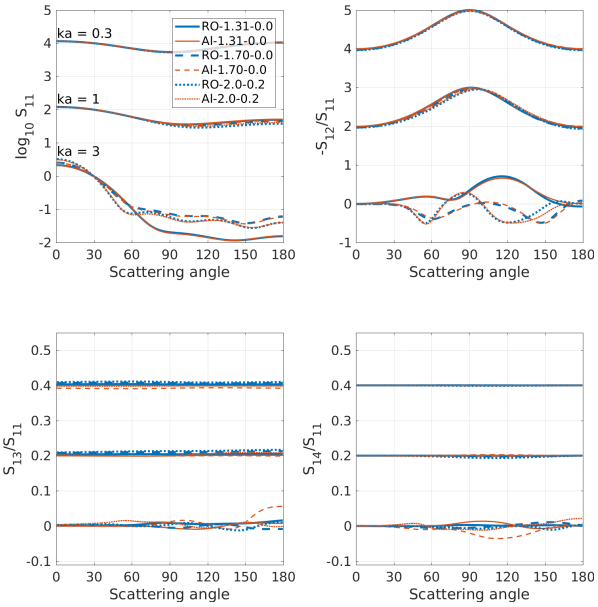

Figure 11: As in Figure 7, but for the 15 deformed ellipsoids only.

Table 6: Same as Table 2, but for only the deformed ellipsoids

$n\backslash ka$	0.3	1.0	3.0
1.31+i0.0	-4.692	-1.759	0.805
1.7+i0.0	-4.057	-1.042	1.263
2.0+i0.2	-3.792	-0.765	0.980

of the scattering matrix components $S_{ij}(\theta, \varphi)$. The level of alignment affects all components similarly, with imperfect alignment flattening the variations in both θ and φ directions when compared to the perfectly aligned case.

In all cases, the intensity comparison results in slight changes with respect to the to level of alignment. From Tables 3–6 we also see, that the more aligned smaller prolate spheroids result in higher scattering cross sections. Also, as size parameter grows, so do the differences in the relative intensities. The $\pm 45°$ and the circular polarizations show higher relative differences in all size parameters, with more varying levels in the imperfectly aligned case, and some systematic changes in the increasing size parameter direction.

The effect of the level of alignment is analysed in Figure 15 for the case $n = 1.7 + \mathrm{i}0.0$, $ka = 3$, where many differences are visible. Generally, the imperfectly aligned case shows similar angle dependencies, with less detail and level of polarization. The ellipsoids and prolate spheroids result in similar polarizations in both alignment states. Spheres and oblate spheroids show similar features to each other in the highly imperfectly aligned case. All perfectly aligned non-spherical shapes exhibit similar angle dependencies in the S_{13}/S_{11}- and S_{14}/S_{11}-components. The similarities are lost with a correlation to the alignment level in the imperfectly aligned case.

6. Conclusions

We found in our study of internal alignment that monochromatic illumination will align particles in large quantities for size parameter $ka \approx 3$ regardless of shape. The smaller size parameters exhibit internal alignment mostly for the prolate spheroid base shape. Such size-dependent alignment efficiency behavior has been demonstrated using semi-analytical methods [6]. The refractive index has a significant effect on the general shape of scattering matrix components, but, as is expected, the only systematic effect of imperfect internal alignment is visible only as the flattening of the components.

We also explicitly showed that internal alignment affects polarization in the ensemble level for single scattering. In addition, the level of alignment in the ensemble, the composition and shape of the dust, and even the alignment direction are visible in the polarization. The setup, while reduced in the sense of modeling real environments, can be used to

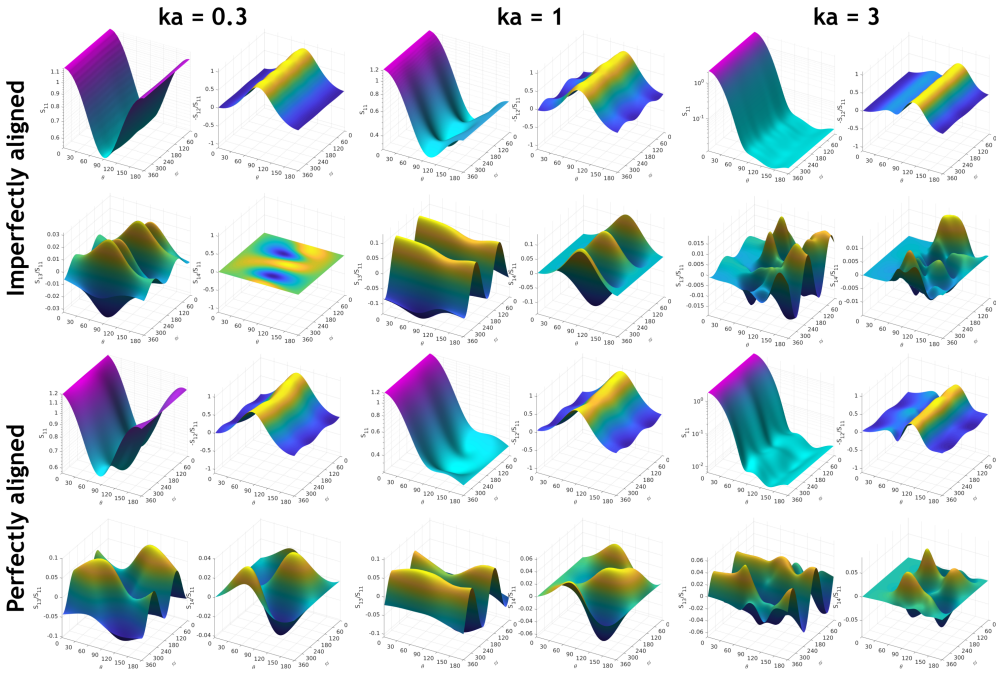

Figure 12: Sheets of the scattering matrix elements as functions of θ and ϕ for the whole ensemble with refractive index $n = 1.31 + \mathrm{i}0.0$, representing ice. The sheet is scaled as flattened, if the maximum deviation from zero is less than 0.01.

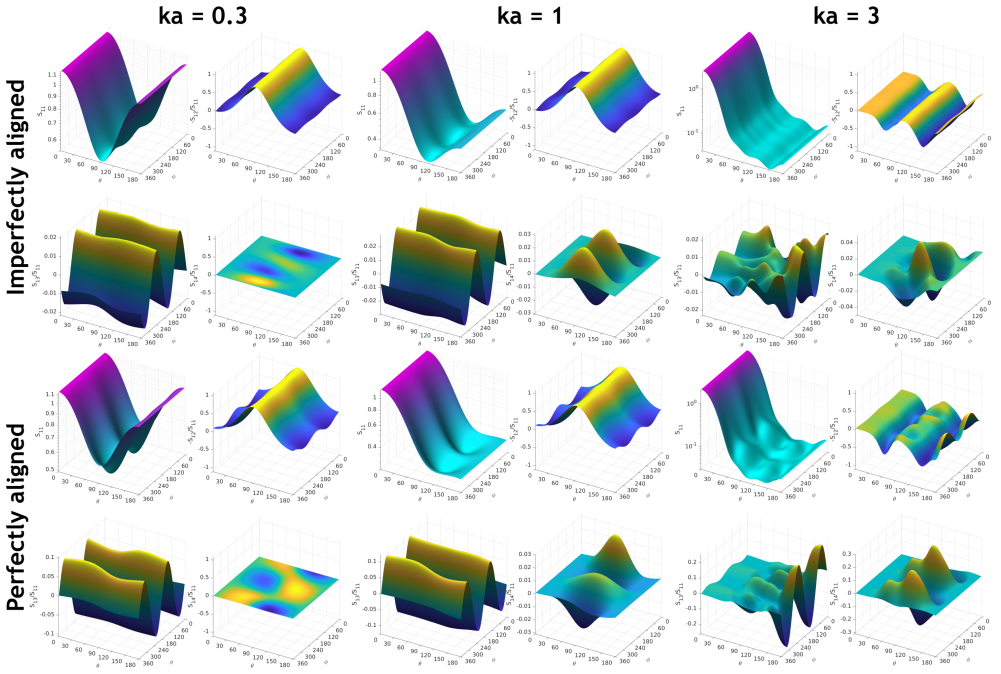

Figure 13: As in Figure 12, but for $n = 1.7 + \mathrm{i}0.0$.

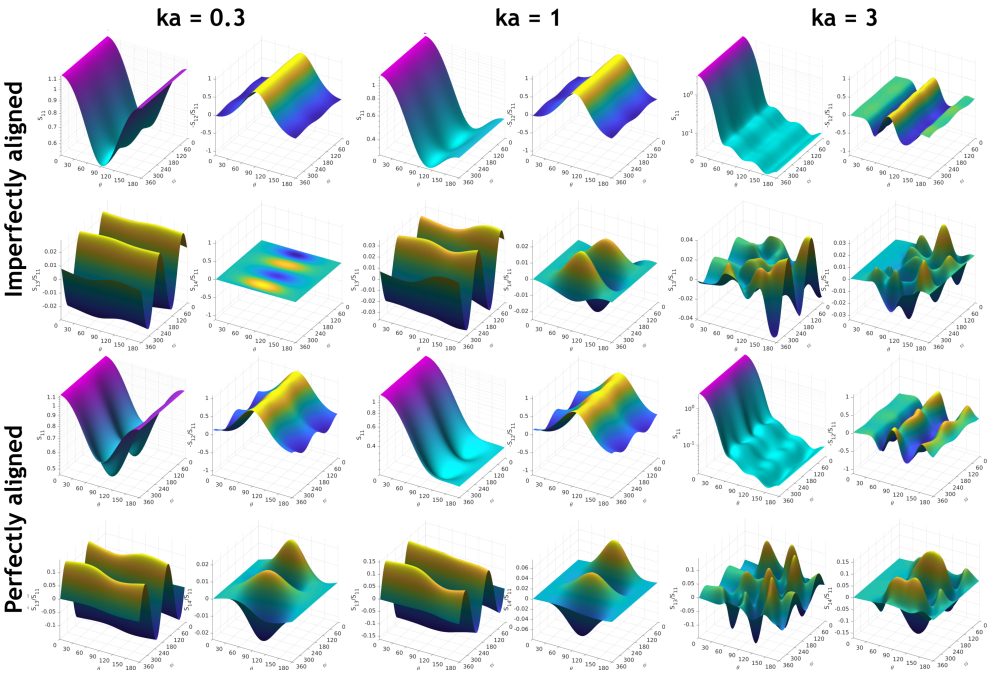

Figure 14: As in Figure 12, but for $n = 2.0 + \mathrm{i}0.2$.

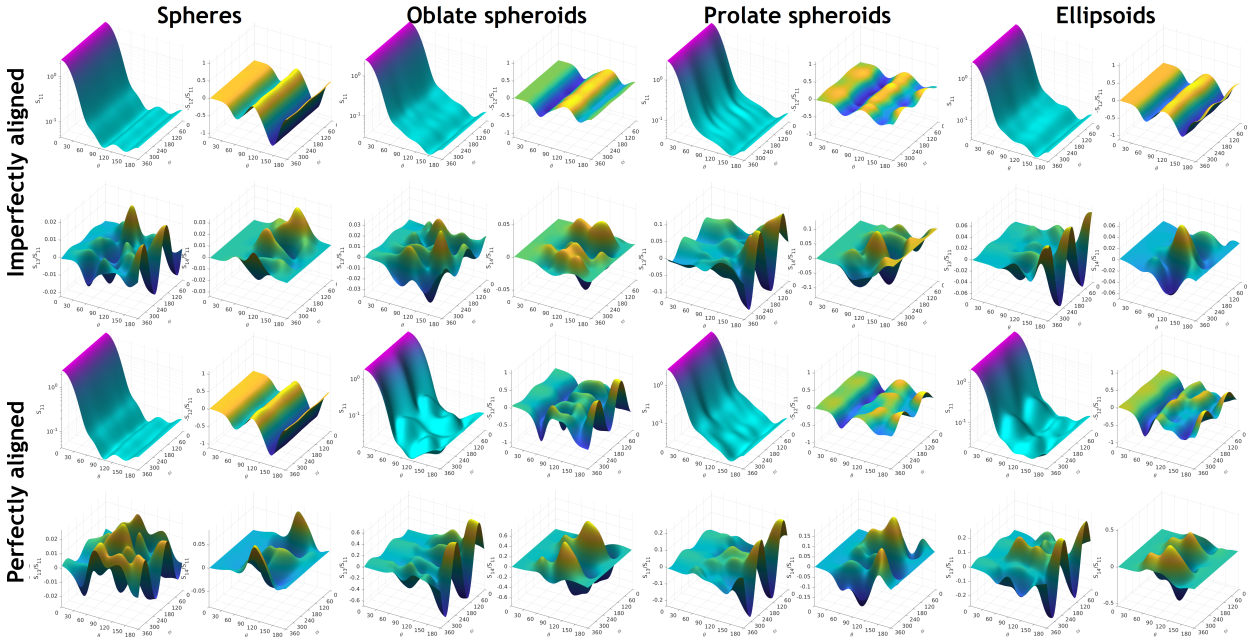

Figure 15: Effect of alignment level on polarization for the case $n = 1.7 + \mathrm{i}0.0$, $ka = 3$.

understand the polarization of large dust particles, whose dissipation of angular momentum is weak.

The methodology presented in this work can also be applied for solving scattering in more realistic environments, in order to understand for example the implications of astrophysical conditions on polarization. This is possible by modeling realistic forces during the dynamical simulation, and by considering particles in a realistic illuminating radiation. Also, the studying of dynamical quantities for the ensemble, such as the stable points of the angular velocity in 3D space, is efficient in our method, needing only small additions in current implementations.

Acknowledgements

The research has been supported, in part, by the ERC grant 320773 (SAEMPL) and the Academy of Finland grant 298137. We acknowledge the CSC for computing resources. The CSC is the Finnish IT center for science and is owned by the Ministry of Education.

References

[1] R. Adam, et al., Planck 2015 results. X. Diffuse component separation: Foreground maps, Astron. Astrophy. 594 (2016) A10. arXiv:1502.01588.

[2] J. S. Hall, Observations of the Polarized Light from Stars, Science 109 (1949) 166.

[3] W. Hiltner, Polarization of Light from Distant Stars by Interstellar Medium, Science 109 (1949) 165.

[4] L. J. Davis, J. L. Greenstein, The Polarization of Starlight by Aligned Dust Grains, Astrophysical Journal 114 (1951) 206–240.

[5] B. Draine, J. Weingartner, Radiative Torques on Interstellar Grains. II. Grain Alignment, Astrophysical Journal 480 (2). doi:10.1086/304008.

[6] A. Lazarian, T. Hoang, Radiative torques: Analytical Model and Basic Properties, Monthly Notices of the Royal Astronomy Society 378 (3) (2007) 910–946. doi:10.1111/j.1365-2966.2007.11817.x.

[7] T. Hoang, A. Lazarian, Grain Alignment by Radiative Torques in Special Conditions and Implications, Monthly Notices of the Royal Astronomy Society 438 (2014) 680–703.

[8] B.-G. Andersson, A. Lazarian, J. E. Vaillancourt, Interstellar Dust Grain Alignment, Annual Review of Astronomy and Astrophysics 53. doi:10.1146/annurev-astro-082214-122414.

[9] K. Muinonen, T. Nousiainen, P. Fast, K. Lumme, J. Peltoniemi, Light scattering by gaussian random particles: Ray optics approximation, Journal of Quantitative Spectroscopy and Radiative Transfer 55 (5) (1996) 577 – 601, light Scattering by Non-Spherical Particles. doi:https://doi.org/10.1016/0022-4073(96)00003-9.
URL http://www.sciencedirect.com/science/article/pii/0022407396000039

[10] K. Muinonen, T. Pieniluoma, Light scattering by Gaussian random ellipsoid particles: First results with discrete-dipole approximation, Journal of Quantitative Spectroscopy & Radiative Transfer 112 (11) (2011) 1747–1752.

[11] F. Tonon, Explicit Exact Formulas for the 3-D Tetrahedron Inertia Tensor in Terms of its Vertex Coordinates, Journal of Mathematics and Statistics 1 (1) (2004) 8–11.

[12] T. A. Nieminen, N. du Preez-Wilkinson, A. B. Stilgoe, V. L. Loke, A. A. Bui, H. Rubinsztein-Dunlop, Optical tweezers: Theory and modelling, Journal of Quantitative Spectroscopy and Radiative Transfer 146 (2014) 59–80. doi:10.1016/j.jqsrt.2014.04.003.
URL https://doi.org/10.1016%2Fj.jqsrt.2014.04.003

[13] B. Stout, B. Rolly, M. Fall, J. Hazart, N. Bonod, Laser-particle interactions in shaped beams: Beam power normalization, Journal of Quantitative Spectroscopy and Radiative Transfer 126 (Supplement C) (2013) 31 – 37, lasers and interactions with particles 2012. doi:https://doi.org/10.1016/j.jqsrt.2012.10.007.
URL http://www.sciencedirect.com/science/article/pii/S0022407312004360

[14] J. Stratton, Electromagnetic Theory, Vol. 1, McGraw-Hill Company, 1941.

[15] J. D. Jackson, Classical Electrodynamics, Wiley, 1998, iSBN: 0-471-30932-X.

[16] Ø. Farsund, B. Felderhof, Force, torque, and absorbed energy for a body of arbitrary shape and constitution in an electromagnetic radiation field, Physica A: Statistical Mechanics and its Applications 227 (1-2) (1996) 108–130. doi:10.1016/0378-4371(96)00009-x.
URL https://doi.org/10.1016%2F0378-4371%2896%2900009-x

[17] D. Mackowski, Discrete dipole moment method for calculation of the T matrix for nonspherical particles, Journal of the Optical Society of America A 19 (2002) 881–893.

[18] V. Loke, T. Nieminen, N. Heckenberg, H. Rubinsztein-Dunlop, T-matrix calculation via discrete dipole approximation, point matching and exploiting symmetry, Journal of Quantitative Spectroscopy & Radiative Transfer 110 (14) (2009) 1460–1471.

[19] J. Markkanen, P. Ylä-Oijala, A. Sihvola, Discretization of the volume integral equation formulation for extremely anisotropic materials, IEEE Transactions on Antennas and Propagation 60 (11) (2012) 5195–5202.

[20] J. Markkanen, A. Yuffa, Fast superposition T-matrix solution for clusters with arbitrary-shaped constituent particles, Journal of Quantitative Spectroscopy & Radiative Transfer 189 (2017) 181–188.

[21] C. Choi, J. Ivanic, M. Gordon, K. Ruedenberg, Rapid and stable determination of rotation matrices between spherical harmonics by direct recursion, The Journal of Chemical Physics 111 (19) (1999) 8825–8831.

[22] C. Bohren, D. R. Huffman, Absorption and Scattering of Light by Small Particles, Wiley Science Paperback Series, 1998.

[23] H. C. van de Hulst, Light Scattering by Small Particles, John Wiley and Sons, 1957.

[24] T. Hoang, A. Lazarian, Radiative torque alignment: Essential Physical Processes, Monthly Notices of the

Royal Astronomy Society 388 (1) (2007) 117–143. doi:10.1111/j.1365-2966.2008.13249.x.

[25] J. Herranen, J. Markkanen, K. Muinonen, Dynamics of small particles in electromagnetic radiation fields: A numerical solution, Radio Science 52. doi:10.1002/2017RS006333.